Tuning the Optical and Structural Properties of Halide Perovskite by PbS Quantum Dot Additive Engineering for Enhanced Photovoltaic Performances

Kunnummal Mangott Muhammed Salim, Loreta A. Muscarella, Imme Schuringa, Ramses Alejandro Miranda Gamboa, Jeevan Torres, Carlos Echeverría-Arrondo, Andrés F. Gualdrón-Reyes, Jhonatan Rodriguez-Pereira, Marina E. Rincon, Bruno Ehrler, Iván Mora-Seró,* and Sofia Masi*

The combination of inorganic PbS quantum dots (QDs) and lead halide perovskite in one nanocomposite is considered as a promising approach to overcoming the limitations of metastable perovskites. However, to date, only a few examples of improved optoelectronic perovskites are realized with such materials. One of the keys to unraveling the full potential offered by the PbS QDs/perovskite material is the ability to purposefully modulate the interfacial electronic energy levels by changing the PbS QDs capping shell. Herein, this approach to adjust the offsets of the energy levels of the perovskite is demonstrated. To prepare the perovskite films with embedded PbS QDs, the organic capping of QDs is exchanged by a halide perovskite shell. Film properties are correlated to the structural changes of the soft perovskite matrix and their optical properties. Interestingly, this approach can be used to adjust the energy levels in the whole nanocomposite film, without changing the original bandgap, and thus paves the way for novel functional materials for optoelectronic devices. The applicability of this method is exemplified by fabricating solar cells with the perovskite nanocomposite, observing that the introduction of PbS/FAPI QDs into FAPI matrix boosts the average performance from 17.9% to 18.9% (21.3% champion device).

1. Introduction

Solar cells from the emerging halide perovskites (HPs) are the most promising and efficient potential successors to the existing nonrenewable energy harvesters. This stems from their facile and low-cost fabrication methods at various atmospheric conditions that contend with the existing silicon photovoltaics.[1] Moreover, their favorable properties like higher absorption coefficient, tunable bandgap, low exciton binding energy, high charge carrier mobility, and defect-tolerant nature have a positive impact on the use of HPs in several optoelectronic applications.[2]

Recently, PbS quantum dots (QDs) have been used as an external additives[3] to control the growth and stabilization of methylammonium lead iodide (MAPI)[4] and the metastable HPs like formamidinium lead iodide (FAPI) and cesium lead iodide

K. M. M. Salim, R. A. Miranda Gamboa, J. Torres, C. Echeverría-Arrondo, A. F. Gualdrón-Reyes, I. Mora-Seró, S. Masi
Institute of Advanced Materials (INAM)
University Jaume I
Avenida de Vicent Sos Baynat, s/n, 12071 Castelló de la Plana, Castellón, Spain
E-mail: sero@uji.es; masi@uji.es

K. M. M. Salim
Institut Photovoltaïque d'Île-de-France (IPVF)
18 Boulevard Thomas Gobert, 91120 Palaiseau, France

L. A. Muscarella, I. Schuringa, B. Ehrler
Center for Nanophotonics
AMOLF
Science Park 104, 1098 XG Amsterdam, The Netherlands

L. A. Muscarella
Department of Chemistry
Utrecht University
Princetonlaan 8, 3584 CB Utrecht, The Netherlands

R. A. Miranda Gamboa, M. E. Rincon
Instituto de Energías Renovables
Universidad Nacional Autónoma de México
Privada Xochicalco S/N, Temixco, Mor. C.P. 62580, México

A. F. Gualdrón-Reyes
Facultad de Ciencias
Instituto de Ciencias Químicas, Isla Teja, Universidad Austral de Chile
Valdivia 5090000, Chile

J. Rodriguez-Pereira
Center of Materials and Nanotechnologies
Faculty of Chemical Technology
University of Pardubice
Nam. Cs. Legii 565, Pardubice 53002, Czech Republic

J. Rodriguez-Pereira
Central European Institute of Technology
Brno University of Technology
Purkynova 123, Brno 61200, Czech Republic

(CsPI) without changing their optical bandgap,[5] and it is evident how the heterointerface plays a pivotal role in energetic stabilization.[5b,6] Although such advancements have been achieved in chemistructural stabilization using PbS QDs, the resulting perovskite composites can still show either advantageous or deleterious optoelectronic properties, depending upon the perovskite composition investigated, the amount of embedded PbS QDs used in the final composition,[4] and the shell between the PbS QDs and the perovskite matrix.[7] The potential for improved efficiency of the corresponding solar cell or other optoelectronic devices shows the promise of these hybrid material combinations.[3a,5a,8]

It is worth noting that, from the perspective of fundamental studies, the PbS–shell–perovskite matrix provides a platform to directly visualize the epitaxial growth in the whole bulk. There have been several advantages by the hybridization of PbS QDs with the perovskite matrix and the lattice mismatch has been identified as an important criterion for the growth and stability.[5] For instance, the all-inorganic metastable HP, CsPI, is shown to have nearly zero lattice mismatch values with the PbS QDs matrix.[5a] The inclusion of PbS QDs helps the generation of seed-like nucleation regions for the growth of high-quality HP absorbers with enhanced phase stability, but also leaves an opportunity to study the charge transfer and optoelectronic behaviors.[9] Significant works concerning the charge transfer in perovskite devices have focused on modifying the work function of conductive electrode materials and thereby minimizing charge injection barriers at the interface with the perovskite.[10] Yet, reports on changes of the HP energy-level positions in the bulk, without changing the bandgap, correlated to a different morphological order of the HP grains/crystals are limited. This is due to the lack of control at the morphological level of the HP growth. In fact, the dual ionic and covalent nature of the HPs bonds makes them prone to uncontrolled growth and easy mechanical deterioration under the imbalance between compressive and tensile strains, which can lead to HP phase degradation.[11]

In this framework, MAPI and FAPI represent two examples, with substantial structural and in turn optical differences, even when the PbS QDs are used to control their growth. The MAPI matrix intrinsically possesses a residual compressive strain due to a tolerance factor $t < 1$; thus, the more compressive lattice strain (reduction of d space, where d is the interplanar spacing in a crystal, $d(110) = 0.62$ nm, $d(220) = 0.31$ nm)[12] in the MAPI matrix is directly correlated with increased defect density and nonradiative recombination.[13] On the other hand, the existence of a residual tensile strain (increase in d spacing, $d(200) = 0.32$ nm, with a cubic unit cell dimension of ≈ 6.36 Å)[14] in α-FAPI (tolerance factor $t > 1$) triggers the transformation to nonphotoactive yellow δ-FAPI to increase the lattice parameter and relieves the strain in the anisotropic crystal plane.[15] In contrast to strain in the MAPI matrix, the compressive strain (i.e., with PbS QDs in the matrix) hinders the transition of cubic α-FAPI to hexagonal δ-FAPI.[5b,6,11b,15,16]

On this basis, developing one material having both the structural features, the desired bandgap, and the suitable energy alignment should be significantly advantageous for perovskite solar cells (PSCs). Therefore, it is of great interest to study how to exploit the structural stability along with the promotion

of the charge transport and reduction of the energy losses in these systems and how this depends upon the PbS–capping shell when the QDs are embedded in these matrices.[7a] As commented earlier, this is quite challenging due to the complexity of optimizing the energy band structures of several layers, and studies associated with the modification of energy offset level in the bulk, avoiding the addition of extra interlayers, are still under represented. At the same time, it should be feasible to prepare nanocomposite films where PbS QDs are properly embedded into the HP matrix. In this context, note that, as-synthesized PbS QDs are capped with organic ligands that prevent them from dissolving into the HP precursor solution that is used for the spin-coating process. This problem is commonly solved by a ligand exchange where the organic capping is replaced by a HP shell.[4,5]

In this work, the structural, optical properties, and the interfacial energy-level alignment have been accordingly determined for six scenarios. They are FAPI and MAPI matrices with no PbS QDs, PbS QDs with FAPI shell (FAPI–PbS), and MAPI shell (MAPI–PbS) in both FAPI and MAPI matrices, in order to highlight the role of shell capping interlayers in tuning the crystal phase growth, strain, and energy-level positions, with the photoluminescence (PL) features, and ultimately to the PSC performances. Firstly, we found that the FAPI–PbS and MAPI–PbS shells induce compressive strain in the FAPI matrix corroborated by the shift of diffraction Bragg peaks to the higher 2θ and blueshift of Raman spectra, respectively. In contrast, the shifting of Bragg peaks to the lower 2θ and redshift of the Raman spectra are observed for the MAPI matrix, indicating the lattice expansion/distortion by the inclusion of PbS QDs. In the electron backscatter diffraction (EBSD) measurements we see that inclusion of PbS QDs in the FAPI matrix leads to an increased alignment of the (111) crystal plane with the sample surface. Interestingly, both FAPI and MAPI matrices showed different photophysical properties with FAPI–PbS and MAPI–PbS inclusions. All films with FAPI matrix are found to suffer from the nonradiative recombination centers by photogenerated charge transfer to PbS QDs, which reflected unfavorably on the optical properties. In contrast, enhanced photophysical properties are observed for all films with MAPI matrix and are substantiated by the reduced nonradiative recombination and better perovskite morphology. Finally, the interfacial energy-level alignment has been experimentally and theoretically determined. The changes in the FAPI matrix energy-level offset in the presence of MAPI–PbS and especially with FAPI–PbS surpass the limitation dictated by the optical properties, thus resulting in higher performance in PSCs. In the case of the FAPI matrix, the balance between the limited optical properties and a slight change in the perovskite bulk energy-level position with FAPI–PbS shell leads to a higher power conversion efficiency of 21%.

2. Results and Discussion

Two types of perovskite shells, FAPI and MAPI, are used to replace the long-chain oleic acid ligands and to make the PbS QDs surface polar in nature, to subsequently mix them into the solvents used for the fabrication of HP thin films. The details regarding the ligand exchange processes are described in the

Supporting Information. The reference names used for the samples are as follows: FAPI matrix (as FAPI), FAPI–PbS in FAPI matrix (as FAPI–PbS–F), MAPI–PbS in FAPI matrix (as MAPI–PbS–F), MAPI matrix (as MAPI), FAPI–PbS in MAPI matrix (as FAPI–PbS–M), and MAPI–PbS in MAPI matrix (as MAPI–PbS–M).

The perovskite phase, crystallographic orientation, and local strain in thin films of FAPI and MAPI matrices with different core/shell PbS QDs were studied by EBSD.[17] EBSD is an SEM-based technique that involves the interaction of the electron beam with a crystalline substance, where the backscattered electrons result in the generation of patterns on a 2D detector, also known as Kikuchi patterns. These patterns arise from incoherent wide-angle electron scattering, specifically thermal diffuse scattering, within the specimen. The acquired Kikuchi patterns provide valuable information regarding the identification of grains, including their size, shape, and the characteristics of the boundaries between them. Through pattern fitting, it becomes possible to determine the crystal phase and grain orientation, and detect strain within the material. The crystal structures used for indexing the Kikuchi patterns are tetragonal (space group $I4/mcm$) for the MAPI matrices and cubic (space group $Pm-3m$) for the FAPI matrices, and in the case of presence of PbI_2, trigonal (space group $P-3m1$). To study the trends in orientation in the FAPI and MAPI matrices as a function of PbS QDs introduction, we combined the data from multiple EBSD scans and reported the results using discrete inverse pole figure (IPF) plots, see

Figure 1 and S1–S2, Supporting Information. These IPF show which planes are aligned perpendicularly to the z-axis of the sample, to the sample normal. The perovskite grains in FAPI, FAPI–PbS–F, and MAPI–PbS–F thin films are randomly oriented with some preferential orientation of the (111) plane parallel to the plane of the sample substrates, see Figure 1a–c. This orientation preference becomes slightly more prominent when the PbS QDs are embedded in the perovskite matrix,[18] considering that PbS nanoparticles introduce seed-like nucleation sites to favor the orientation of perovskite crystals, being beneficial for the carrier transport and the increase of the device performance.[14] We note that not all regions on the film resulted in clear Kikuchi patterns, which means that the preferential orientation could arise either from more regions oriented in the (111) plane or from better data quality from these regions. Previously it was predicted that (111) twin boundaries are relatively stable in FAPI perovskite and do not induce electron- or hole-trapping states at these grain boundaries.[18,19] The absence of major changes in the crystal orientation upon inclusion of PbS QDs in the FAPI maps is in agreement with the X-ray diffraction (XRD) patterns. Apparently, the dominating (100) peak in the XRD patterns could be explained by the fact that the XRD patterns give an average across the bulk, whereas EBSD probes at the surface.

The discrete IPF plots of the thin films with MAPI matrix (Figure 1d–f) show a different trend with the inclusion of QDs in comparison to those with the FAPI matrix. The films
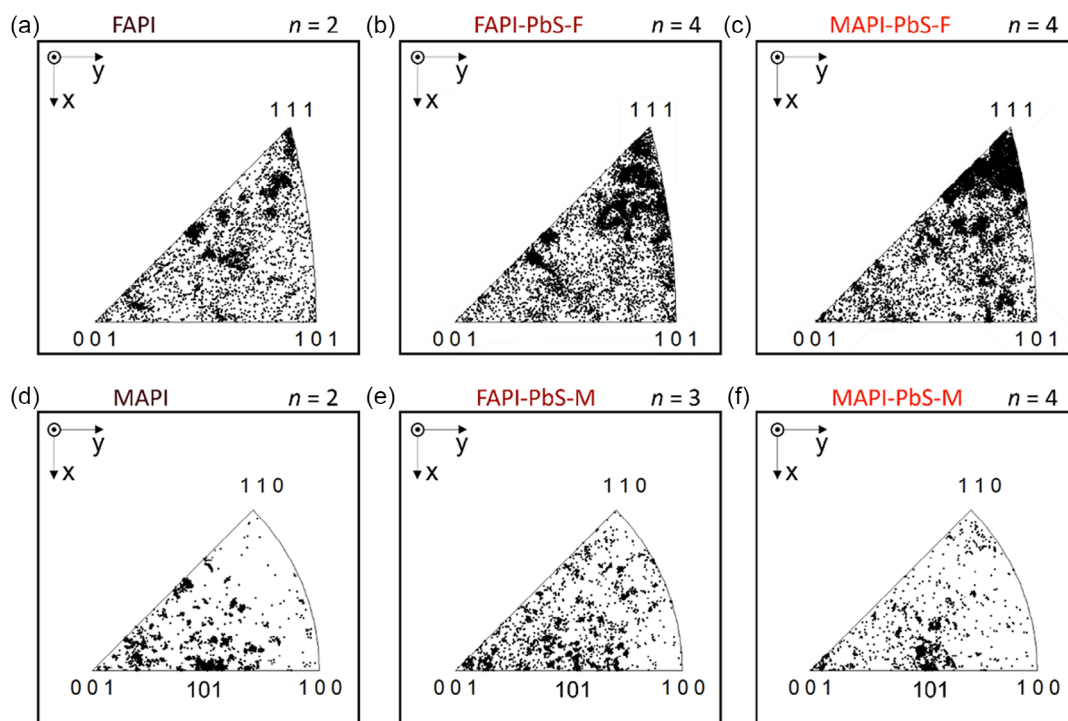

Figure 1. Discrete IPF plots of multiple maps per composition to show the change in orientation along z-axis with inclusion of PbS QDs in the FAPI/MAPI matrices. Every point in the orientation map that was reliably indexed (CI > 0.1) is represented by a point in the discrete IPF plot. All plots show the orientation of the inverse pole (normal to a plane) along the z-axis. The number of maps included per discrete IPF plot n is indicated at the top right of each subplot. a–c) IPF discrete plots of FAPI (a), FAPI–PbS–F (b), and MAPI–PbS–F (c), all indexed with the cubic crystal structure of FAPI (Pm-3m), and d–f) for MAPI (d), FAPI–PbS–M (e), and MAPI–PbS–M (f), all indexed with the tetragonal crystal structure of MAPI (space group I4/mcm).

show a preferential alignment of the (001) and (101) planes in plane with the sample surface. The FAPI–PbS–M and MAPI–PbS–M films show a very similar orientation pattern compared to MAPI. EBSD mapping can also reveal the microstrain within a perovskite grain.[20] We find the presence of considerable strain in the FAPI grains by observing the gradual color change within various grains in the IPF orientation maps, see Figure S1a–d, Supporting Information. In all FAPI films, we find grains with a strain up to 6°, with outliers of 16°, see Figure S3 and S4, Supporting Information. Histograms of the grain orientation spread (GOS) values from all maps per composition, see Figure S5, Supporting Information, show that the inclusion of PbS QDs does not lead to a change in strain within grains for the FAPI-based films nor the MAPI-based films. Based on the GOS histograms, the difference in the average strain between the films with FAPI and MAPI matrix seems limited, see Table S1, Supporting Information, but the FAPI-based films contain multiple heavily strained grains. Due to the limited number of grains measured, a more detailed investigation is necessary to confirm this trend.

We further studied the perovskite crystallinity, structural changes, and lattice strain effects in the thin films of FAPI and MAPI matrices with FAPI–PbS and MAPI–PbS QDs by XRD and Raman spectroscopy. As shown in Figure S6a, Supporting Information, the reference FAPI, FAPI–PbS–F, and MAPI–PbS–F perovskite films showed almost identical XRD patterns with the presence of remnant PbI_2 (12.70°) and δ-FAPI phase (11.80°).[6] The diffraction Bragg peaks at 13.98°, 19.84°, 24.34°, 28.13°, 31.52°, 34.68°, 40.24°, and 42.78° in all spectra correspond to (100), (110), (111), (200), (210), (211), (220), and (221) crystal planes and are related to the cubic, space group *Pm-3 m*, crystalline black phase of FAPI (α-FAPI). The FAPI–PbS–F and MAPI–PbS–F films showed a slight shift to a higher 2θ angle for the (100) and (200) diffraction Bragg peaks with relatively broader width when compared to FAPI film, see **Figure 2**a,b.
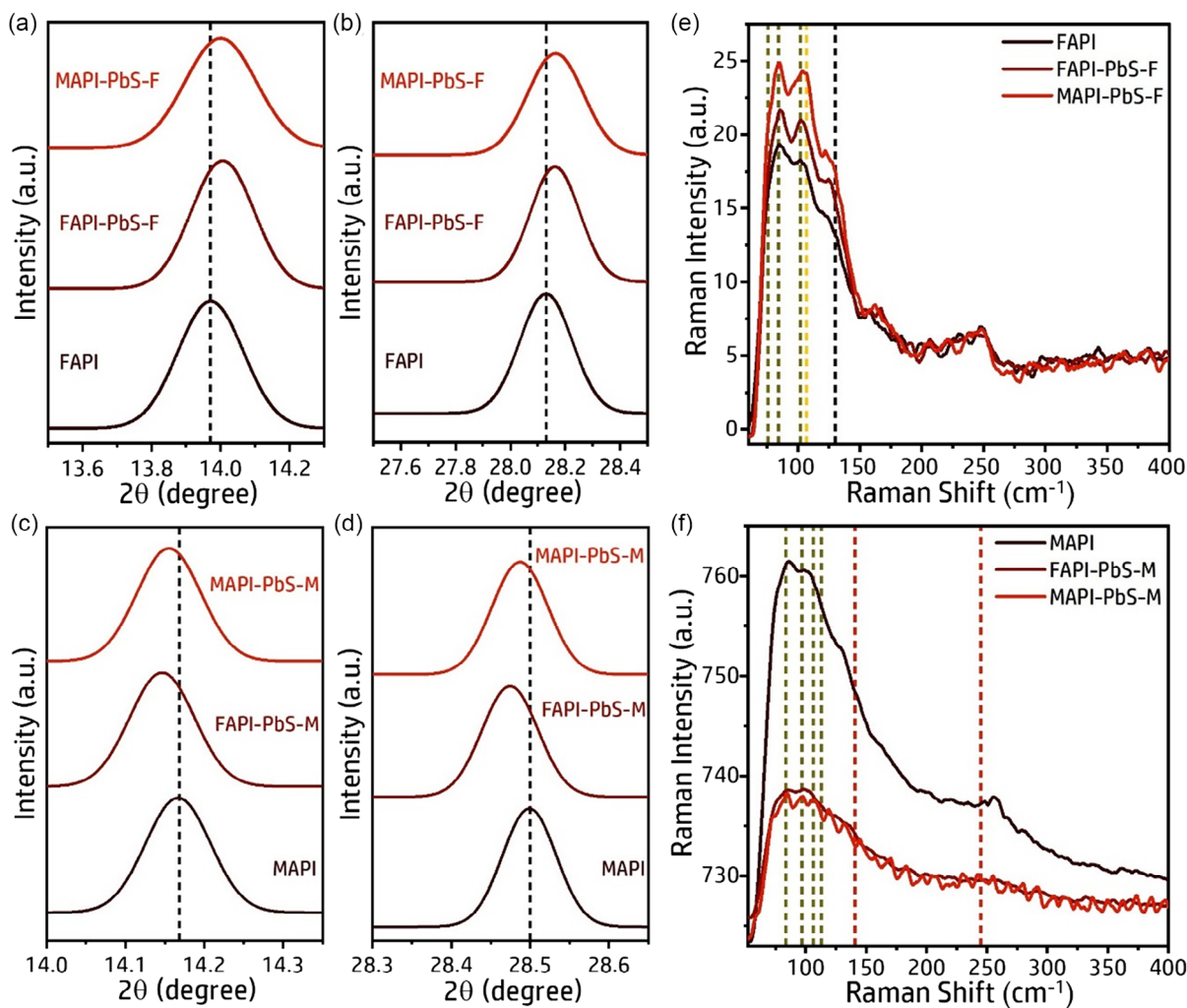
Figure 2. The Gaussian fit of the magnified XRD Bragg peaks: a) (100) and b) (200) of FAPI, FAPI–PbS–F, and MAPI–PbS–F thin films. The Gaussian fit of the magnified diffraction Bragg peaks, c) (110) and d) (220) of MAPI, FAPI–PbS–M, and MAPI–PbS–M thin films. The corresponding Raman spectra of e) FAPI, FAPI–PbS–F, and MAPI–PbS–F, f) MAPI, FAPI–PbS–M, and MAPI–PbS–M-based perovskite thin films. The Raman spectra are shown without any spectral correction or normalization and the vertical lines indicate spectral mode assignment: green lines correspond to vibrations of the inorganic [PbI₆] cage, yellow lines to δ-FAPI phase, black lines to α-FAPI, and red lines to vibrational and torsional mode of the MA cation in MAPI.

This is an indication of lattice contraction by the generation of local compressive microstrains in the matrix offered by embedded PbS QDs, with smaller lattice parameters than perovskite; thus, it signifies a heteroepitaxial growth of FAPI epilayer by the templating effect of PbS QDs through chemical and structural benefits.[5b] This is in agreement with the lattice contraction of the FAPI matrix under the influence of compressive strain due to the smaller PbS lattice parameter and the subsequent stabilization mechanisms reported earlier.[5b,11b] As shown in Figure S6b, Supporting Information, the reference MAPI, FAPI–PbS–M, and MAPI–PbS–M perovskite films showed similar crystalline XRD patterns with the presence of remnant PbI$_2$ (12.70°).[21] The diffraction Bragg peaks at 14.18°, 20.08°, 24.56°, 28.50°, 31.93°, 40.73°, and 43.26° in all spectra referred to (110), (112), (202), (220), (310), (224), and (314) are related to the room-temperature tetragonal (space group of $I4/mcm$) crystalline phase of MAPI. Contrary to the FAPI-based films, the FAPI–PbS–M and MAPI–PbS–M films showed a slight shift to lower 2θ angle for the (110) and (220) diffraction peaks when compared to MAPI film, see Figure 2c,d. This is an indication of lattice expansion/distortion by the generation of local tensile microstrains in the matrix offered by embedded PbS QDs. This lattice expansion under tensile strain is in agreement with the previously reported works on FAPI and MAPI matrix.[11b,c] The shift in the diffraction Bragg peak position signifies the stress induced by PbS QDs (FAPI–PbS or MAPI–PbS) and is responsible for the homogenous spreading of the strain during the perovskite crystalline growth.

Raman vibrational modes are susceptible to external strains, which can help to illustrate the stress levels in the perovskite material.[6,11b] Figure 2e shows the Raman spectra of FAPI, FAPI–PbS–F, and MAPI–PbS–F perovskite thin films, respectively. All the Raman spectra possess relatively similar Raman vibrational modes.[6] As shown in Figure 2e, low-wavenumber shoulder below 100 cm^{-1} and extending to 70 cm^{-1} is present from the vibrations of the inorganic [PbI$_6$] cage, in addition to the contribution from the secondary phases, that is, PbI$_2$ phonon modes, as green vertical lines in Figure 2e. A relatively small vibrational mode at 107 cm^{-1} denotes the presence of δ-FAPI, yellow vertical line in Figure 2e. A broader Raman band positioned at 120–138 cm^{-1}, which is from the stretching of the lead–iodine bond and in-plane bending of FA cations,[6,11b] signifies the presence of the α-FAPI phase, as black vertical lines in Figure 2e. In addition, the presence of Raman modes at 165 and 241 cm^{-1} comes from the oxygen-related compounds at the surface, that is, Pb—O chemical bond nature.[6]

Depending on the nature of the strain, the Raman spectra can undergo peak broadening, shifting, and splitting due to the changes in bond rigidity of different perovskite phases.[11b] Compressive strain results in the broadening and enhanced intensity of the Pb–I peaks. The peak at around 122 cm^{-1} in Figure 2e, which indicates the stretching of the Pb–I bond, increases in intensity and slightly broadens for FAPI–PbS–F and MAPI–PbS–F when compared to the reference FAPI matrix. Usually, the symmetrical cubic structure of FAPI matrix is relatively less Raman active and broad in comparison to other perovskite phases of FAPI.[22] However, the presence of FAPI–PbS and MAPI–PbS in the FAPI matrix imparts the local compressive strain and causes the lattice contraction of the inorganic

framework and results in the relatively higher Raman signal with slight splitting of the peak. The peak is found to be blueshifted to higher wavenumbers for the case of FAPI–PbS–F and MAPI–PbS–F, see Figure S7a,b, Supporting Information, for the deconvolution plots.

In the case of the MAPI matrix, the Raman vibrational spectra are shown in Figure 2f, it shows the main fingerprints of both highly ordered inorganic cage (I–Pb–I bending and stretching modes) and vibrational modes of organic cations.[23] The vibrational modes at lower wavenumber, that is, at 70, 96, 106, and 113 cm^{-1}, contribute to the vibrations of inorganic [PbI$_6$] cage.[23a] The vibrational modes of the organic cations (methylammonium, MA) are present at the broad range of 100–190 cm^{-1}, a peak at 134 cm^{-1} constitutes the vibrational mode of the MA cation (red vertical line in Figure 2f).[23] A broad intense band at 243 cm^{-1} is attributed to the organic MA cation torsional mode (red vertical line in Figure 2f).[23b] As shown in Figure 2f, all the Raman spectra of MAPI, FAPI–PbS–M, and MAPI–PbS–M show the vibrational modes of the tetragonal phase.[23a] The Raman spectra of MAPI are strong and very distinguishable in pattern, this is due to the presence of Raman active tetragonal crystalline phase.[22] However, in the case of FAPI–PbS–M and MAPI–PbS–M systems, the Raman signals are relatively weak and broad. The Raman modes at 243 cm^{-1}, torsional mode of MA cation, are found to be broader and redshifted to a lower wavenumber when compared to pure MAPI matrix, see Figure S7c,d, Supporting Information. The redshift of Raman mode and the lower peak intensity signify a small lattice expansion in the FAPI–PbS–M and MAPI–PbS–M matrix by the inclusion of PbS QDs, since the lattice expansion offers a large orientational mobility for the MA cations in the matrix.[24] This is in agreement with the XRD pattern shift to the lower 2θ angles, as shown in Figure 2c,d. From the combined XRD and Raman spectra studies, the templating effects of FAPI–PbS and MAPI–PbS QDs in HPs composite materials, that is, established in terms of compressive and tensile strain in FAPI and MAPI matrix-based thin films, respectively, are corroborated. The compressively phase-stabilized (FAPI case) or strain-relaxed (MAPI case) films have a huge impact on the material phase stability, photophysical properties, and PSC applications.

In order to further investigate the structural distortions, we have performed ab initio simulations, see the theoretical Section 1 in the Supporting Information for further details. To assess the structural distortions in the matrix, we have computed four unit cells, MAPI–PbS–M, FAPI–PbS–M, MAPI–PbS–F, and FAPI–PbS–F, composed of a perovskite matrix and an embedded PbS QD of 17 Å in diameter and shape approximately spherical. **Figure 3** depicts their atomic structures with indication of the [PbI$_6$] octahedra. We recall that FAPI–PbS–M stands for MAPI matrix with a PbS QD coated with a single layer of FAPI. The calculated volumes in the unit cells are, in increasing order, 31,57 Å^3 for MAPI–PbS–M, 32,06 Å^3 for FAPI–PbS–M, 32,28 Å^3 for MAPI–PbS–F, and 32,74 Å^3 for FAPI–PbS–F. These values follow the same expansion trend of the clean unit cells without PbS QD, which are 31,38 Å^3 for MAPI and 32,49 Å^3 for FAPI, with an increase of 3.5%. In addition, the atomically resolved perovskite structures highlight the distortions occurring in the Pb–I crystal network. In FAPI matrices with cubic Pm-$3m$ symmetry, the PbI$_6$ octahedra are not rotated, as shown in
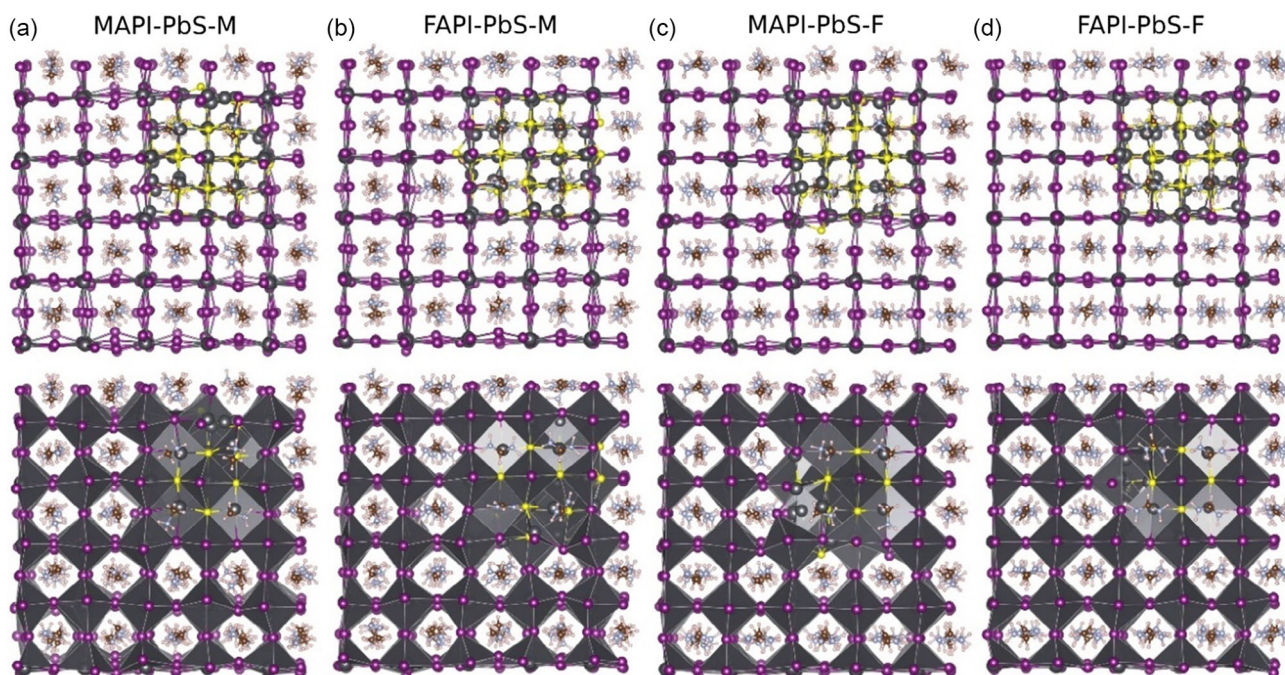
Figure 3. Computed unit cells in the bulk perovskites of a) MAPI–PbS–M, b) FAPI–PbS–M, c) MAPI–PbS–F, and d) FAPI–PbS–F. We note that real samples contain greater and sparser PbS QDs.

Figure 3d. However, in MAPI matrices with tetragonal $I4/mcm$ symmetry, the PbI_6 octahedra are rotated, see Figure 3a. For MAPI perovskite, the R_4^+ rotational distortion mode yields a phase transition from cubic to tetragonal. This phase transition occurs upon reducing the temperature from an aristotype structure with no tilt to a less-symmetric hettotype structure characterized by octahedral tilting.[25]

The structural characterization above clearly defines the role of the PbS, but the effect of the shell is subtler. From the morphological point of view, some differences related to the PbS shell can be found. See Figure S8, Supporting Information, for the comparison of the scanning electron microscopy (SEM) images of FAPI and MAPI matrix-based perovskite thin films. In detail, FAPI–PbS and MAPI–PbS QDs induce the formation of slightly bigger perovskite domain sizes. As shown in Figure S8a, Supporting Information, the FAPI–PbS–F results in comparatively bigger HP crystalline domains (mean size of 600 nm), with similar crystallographic orientation, than the FAPI and MAPI–PbS–F systems without any presence of pinholes, see Figure S8c, Supporting Information, for the HP crystal domain statistical plot. The film topology for all three FAPI matrix films shows the presence of remnant PbI_2 crystallites which is in agreement with the impurity peak observed in the XRD patterns, see Figure S6a, Supporting Information.[6] In the same way, the FAPI–PbS–M shows larger perovskite crystalline domains, mean size of 350 nm, in comparison with MAPI and MAPI–PbS–M counterparts, see Figure S8b,d, Supporting Information.

X-ray photoelectron spectroscopy (XPS) measurements were carried out on fresh samples and samples aged in ambient air for 1 month, to obtain information about their stability. Through survey spectra, see Figure S9, Supporting Information, we identify the presence of C, N, O, S, Pb, and I elements in the perovskite materials. Their chemical composition is summarized in Table S2, Supporting Information. In all the films, high-resolution (HR)-XPS I $3d$ spectra were acquired, see **Figure 4**a,a', showing the typical I $3d_{5/2}$ and $3d_{3/2}$ doublets at 619.1/630.6 eV. These signals are ascribed to the presence of iodide anions in the $[PbI_6]^{4-}$ octahedra coming from the corner-sharing perovskite crystal structure.[26] All fresh FAPI and MAPI films show a I/Pb ratio higher than 3, see Table S2, Supporting Information, indicating an excess of iodine on the material surface. However, after exposing the perovskite films to the environment, differences in composition and composition were dramatic, see Table S3, Supporting Information. All FAPI and MAPI films experience the degradation process, promoting the loss of iodine, associated with MAI and FAI release in the presence of ambient air (H_2O and O_2).[26b,27]

Therefore, oxygenated species can be intercalated along the films to compensate iodide deficiency through the formation of Pb—O bonds, see Table S2–S4, Supporting Information.[26b] However, it is worth noting that the presence of FAPI–PbS shells delays the iodide depletion from both FAPI and MAPI matrices (both FAPI–PbS films showed higher I/Pb ratio compared to the MAPI–PbS equivalent) compared with MAPI–PbS shell, where the highest amount of oxygen was estimated. Then, according to Table S2, Supporting Information, FAPI–PbS–F thin film exhibits the lowest metallic Pb-to-total Pb ratio (Pb^0/Pb_{total}), associated with a lesser density of undercoordinated Pb emerged into the composite material, which stabilizes the black phase. In contrast, the highest Pb^0/Pb_{total} ratio appears in the presence of the MAPI–PbS shell in both the perovskite matrices, as a consequence of a defective perovskite crystal structure. The creation
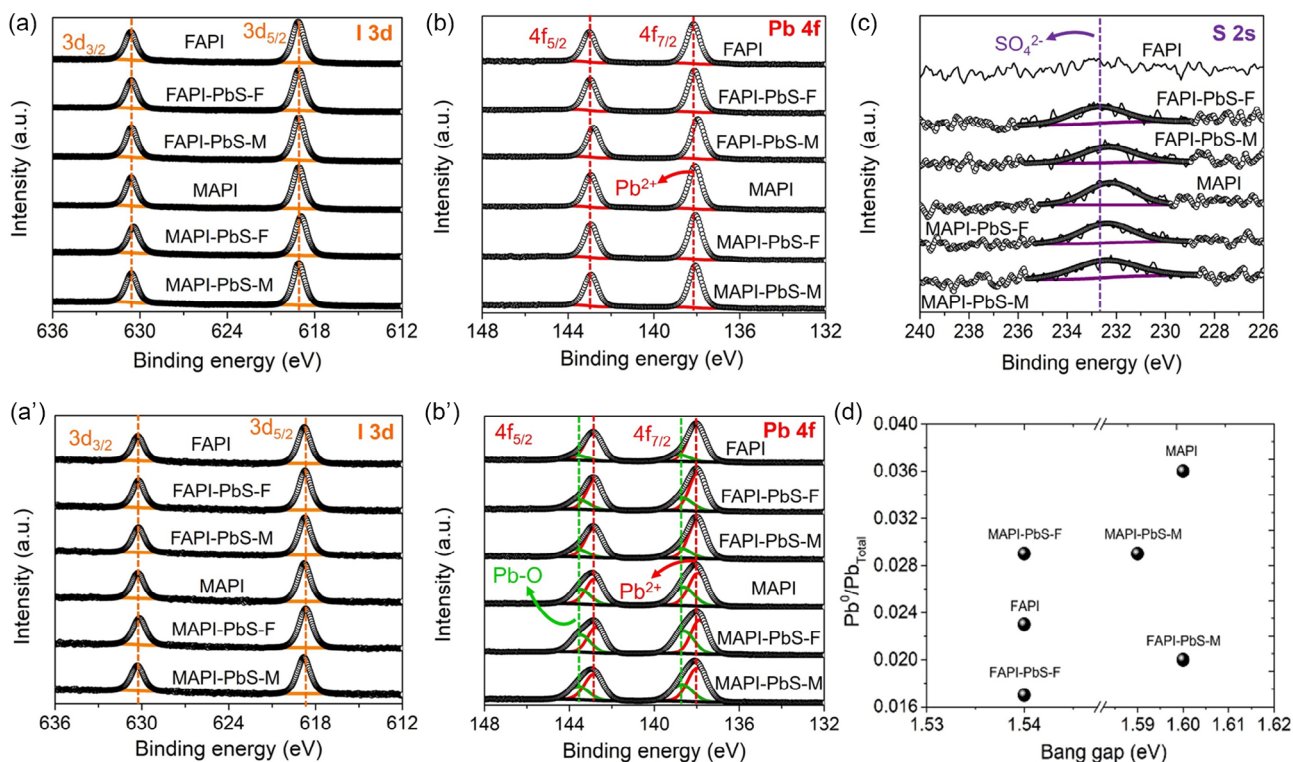
Figure 4. HR-XPS: a,a') I $3d$, b,b') Pb $4f$, c) S $2s$ spectra, d) calculated metallic lead-to-total lead (Pb^0/Pb$_{total}$) ratio versus experimentally observed optical bandgap of FAPI, FAPI–PbS–F, MAPI–PbS–F, MAPI, FAPI–PbS–M, and MAPI–PbS–M-based perovskite thin films. (a,b) Before and (a',b', and c) after 30 days under ambient air aging.

of Pb^0 states into the MAPI and FAPI matrix-based thin films is in line with the emergence of new species into the HR-XPS Pb $4f$ spectra of these materials after exposure to the ambient air, see Figure 4b,b', S10 and Table S2–S4, Supporting Information. Here, a new Pb $4f_{7/2}$/Pb $4f_{5/2}$ doublet appears at 138.8/143.7 eV, attributed to the adsorbed oxygen on the perovskite surface, filling/replacing halide sites and the formation of a I–Pb–O environment.[6,26b,28]

Another reason to favor the stabilization of the FAPI and MAPI thin films is sulfur diffusion from PbS to compensate halide positions. In the presence of FAPI–PbS and MAPI–PbS shells after ambient air exposure, we find the HR-XPS S $2s$ spectra, where a peak was located at ≈ 232.6 eV for FAPI–PbS–F, FAPI–PbS–M, and MAPI–PbS–F, Figure 4c. This signal has been attributed to the existence of SO$_4^{2-}$ species in the modified materials.[29] From this result, we can deduce that PbS QDs are also found in the material surface, passivating the halide deficiency. Moreover, reacting with oxygen and consequently avoiding any fast deterioration, that is, act as a sacrificial additive in the perovskite thin film. By plotting Pb^0/Pb$_{total}$ versus bandgap (Figure 4d), we can relate the ligands to the HP quality/defects. The influence of FAPI–PbS shell in the perovskite matrix hinders the octahedra tilting and presumably delays the iodide release, thus reducing the generation of structural defects. In addition, the oxygen/sulfur incorporation can passivate these states, which eventually would improve the photophysical properties of these perovskite thin films, see below.

We evaluated the ambient air stability of all six analyzed films through monitoring the structural features by XRD. In accordance with the XPS measurements, the presence of PbS QDs stabilizes the FAPI and MAPI matrix. The XRD stability patterns of perovskite thin films fabricated from FAPI–PbS and MAPI–PbS QDs in FAPI and MAPI matrices are compared in Figure S11, Supporting Information. We observed the changes in XRD patterns of the fresh and aged films of FAPI, FAPI–PbS–F, and MAPI–PbS–F. As shown in Figure S11a,b, Supporting Information, the degradation of FAPI film started with the formation of the PbI$_2$ phase (12.70°) in an adequate quantity along with the presence of δ-FAPI phase (11.80°).[6] The relative amount of PbI$_2$ phase has increased for the aged FAPI film. However, the degradation kinetics of perovskite films based on FAPI–PbS–F and MAPI–PbS–F are different than the FAPI film. The decrease of the α-FAPI phase with the slow formation of PbI$_2$ as the degradation products is observed for the thin film of FAPI–PbS–F and MAPI–PbS–F but without the significant formation of δ-FAPI phase. It has been reported that the surface with (111) facet-dominated crystalline FAPI film is less adherent to the moisture, whereas the (100) facet shows enhanced water adhesion tendency and results in an extended lead–iodine bond distance, which lead to the faster PbI$_2$ and δ-phase transitions.[18] Moreover, similar types of degradation pathways are observed for the MAPI matrix-based perovskite thin films. As shown in Figure S11c,d, Supporting Information, a more pronounced formation of the PbI$_2$ impurity phase has been

observed for the case of MAPI and MAPI–PbS–M when compared to the FAPI–PbS–M.

The changes in defect density and strain could affect the optical properties of the perovskite films. Figure S12a,b, Supporting Information, shows the UV–vis absorption spectra of FAPI and MAPI matrices with FAPI–PbS and MAPI–PbS QDs. For the FAPI matrix-based films, all the films showed a similar set of absorption onsets with a redshift for FAPI–PbS–F and MAPI–PbS–F films, see Tauc plot in **Figure 5**a and S12a, Supporting Information. The slight redshift in absorption onset agrees with the trend observed for the FAPI perovskite, where the bandgap has been slightly reduced with the compressive strain.[11b] In the case of FAPI–PbS–M and MAPI–PbS–M, the absorption onset in comparison to the MAPI perovskite matrix is not significantly changed, see Tauc plot in Figure 5b and S12b, Supporting Information.

Moreover, the presence of FAPI–PbS and MAPI–PbS did not significantly affect the PL emission wavelength of FAPI and MAPI matrices, see Figure 5c,d and S12c,d, Supporting Information. Interestingly, the relative PL intensities and the PL time decay of FAPI and MAPI perovskite matrices have been changed with the nature of PbS QD shells. We see a decrease in the PL emission intensity of FAPI–PbS–F and MAPI–PbS–F perovskite film to reference FAPI film considering the absolute photoluminescence quantum yield (PLQY) value of 0.218, 0.147, and 0.138 for FAPI, FAPI–PbS–F, and MAPI–PbS–F, respectively, as shown in Table S5, Supporting Information. This is most probably by a charge transfer that could occur from the perovskite to the PbS QDs due to the favorable bandgap alignment.[5a,7a,9a,30]

However, the enhanced PL emission intensity has been observed for the FAPI–PbS–M and MAPI–PbS–M perovskite film with respect to reference MAPI film. The relative PL intensity of FAPI–PbS–M is higher than the MAPI films. The absolute PLQY values are 0.211, 0.253, and 0.207, for MAPI, FAPI–PbS–M, and MAPI–PbS–M, respectively, as shown in Table S5, Supporting Information. To investigate the charge carrier recombination behaviors in the FAPI and MAPI matrices with FAPI–PbS and MAPI–PbS QDs, the time-resolved PL (TRPL) measurements were further carried out, see Figure 5e,f. The ratio of k_{nr}/k_r ratio is relatively lower for the FAPI–PbS–M and manifests the presence of a few nonradiative channels, which agree with the PLQY (Table S5, Supporting Information). The enhancement of the PL in case of addition of FAPI–PbS QDs in the MAPI matrix could be related to the quasicubic distortion or to the better morphology.[7a,31]

Figure 5e shows the TRPL plots of FAPI, FAPI–PbS–F, and MAPI–PbS–F perovskite thin films. We observe that the decay time (τ) of FAPI (94.9 ns) film is longer than the FAPI–PbS–F (83 ns) and MAPI–PbS–F (21.7 ns). In addition, the average decay time (τ_{avg}) value and PLQY allow for the calculation of radiative (k_r) and nonradiative (k_{nr}) recombination decay rate constants (see Table S5, Supporting Information). The k_r and k_{nr} values are comparatively similar in FAPI and FAPI–PbS–F, but 3–4 times higher in MAPI–PbS–F: k_r values in FAPI ($0.23 \times 10^7 \, s^{-1}$), FAPI–PbS–F ($0.18 \times 10^7 \, s^{-1}$), and
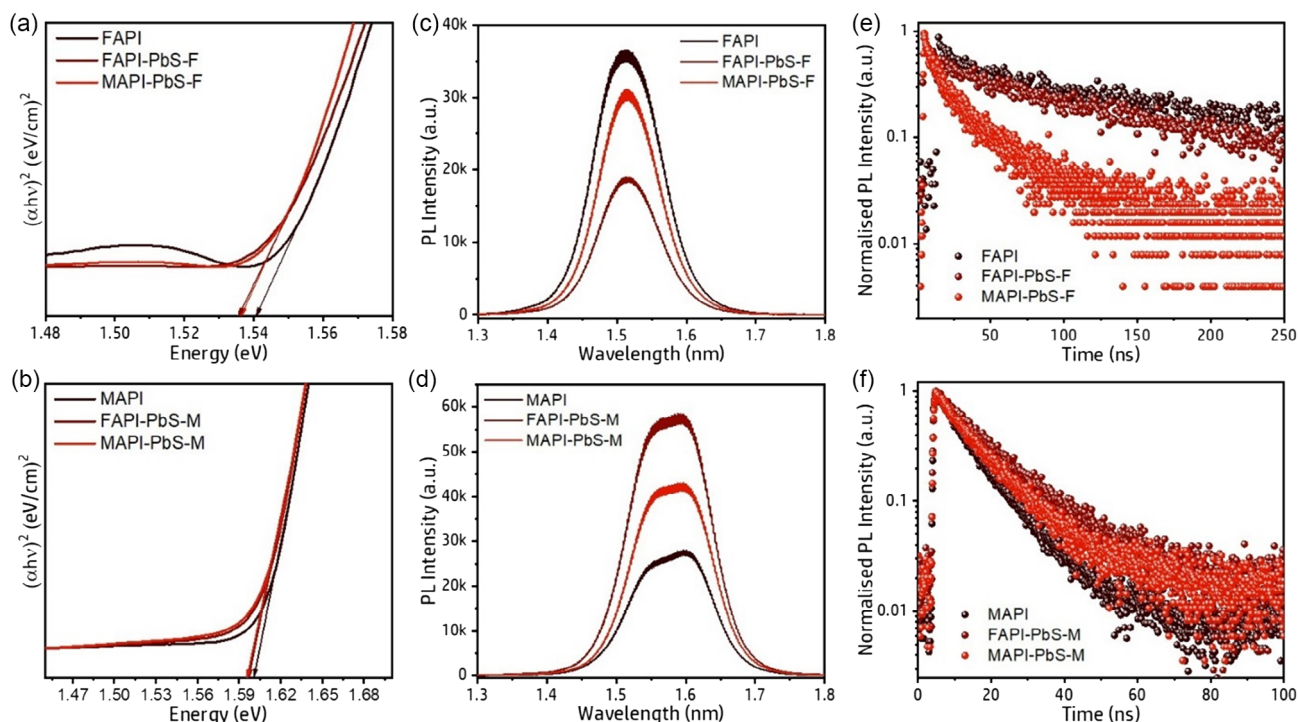
Figure 5. a,b) Tauc plots derived from corresponding UV–vis absorption spectra, c,d) corresponding steady-state PL, and e,f) time-resolved PL (TRPL) spectra of all the analyzed thin films. The derived bandgap values are FAPI (1.540 eV), FAPI–PbS–F (1.535 eV), MAPI–PbS–F (1.536 eV), MAPI (1.600 eV), FAPI–PbS–M (1.596 eV), and MAPI-PbS-M (1.595 eV) respectively.

MAPI–PbS–F ($0.63 \times 10^7 \, s^{-1}$) perovskite thin films, as well as k_{nr} values for MAPI–PbS–F ($3.97 \times 10^7 \, s^{-1}$) FAPI–PbS–F ($1.02 \times 10^7 \, s^{-1}$) and FAPI ($0.82 \times 10^7 \, s^{-1}$). Table S5, Supporting Information, shows the higher k_{nr}/k_r ratio observed for MAPI–PbS–F that can be attributed to the defects or stronger photogenerated energy transfer to the PbS QDs which ultimately act as the nonradiative recombination centers.[30] Figure 5f shows the TRPL plots of MAPI, FAPI–PbS–M, and MAPI–PbS–M perovskite thin films. In line with the PL intensity trend, the FAPI–PbS–M (12.5 ns) film shows a higher average lifetime (τ_{avg}) value when compared to the MAPI–PbS–M (9.7 ns) and MAPI (7.7 ns) films. Similar to the trends observed for the FAPI-based films, Table S5, Supporting Information, shows that k_r values are the highest for MAPI ($2.74 \times 10^7 \, s^{-1}$) and MAPI–PbS–M ($2.13 \times 10^7 \, s^{-1}$), and slightly lower for FAPI-PbS-M ($2.02 \times 10^7 \, s^{-1}$), and this holds also for the k_{nr} values, where MAPI ($10.2 \times 10^7 \, s^{-1}$) and MAPI–PbS–M ($8.17 \times 10^7 \, s^{-1}$), and FAPI–PbS–M ($5.97 \times 10^7 \, s^{-1}$). The ratio of k_{nr}/k_r ratio is relatively lower for FAPI–PbS–M mainly because of the decrease in k_{nr} and manifests the presence of fewer or inefficient nonradiative channels, which well agree with the PL intensity enhancement and with PLQY, see Table S5, Supporting Information. These favorable photophysical properties confer the possibilities of HP nanocomposite materials (both FAPI and MAPI matrix-based thin films) in efficient PSCs, which stem from their better crystallinity and mitigated nonradiative recombinations.

Finally, PSCs have been fabricated by implementing a planar n–i–p device architecture which consists of indium tin oxide (ITO)/SnO$_2$/perovskite (FAPI/MAPI matrices with FAPI-PbS and MAPI-PbS QDs)/2,2′,7,7′-tetrakis(N,N-di-4-methoxyphenylamino)-9,9′-spirobifluorene (Spiro-MeOTAD)/Au, see Figure 6a.[21] All the FAPI matrix-based PSCs were fabricated under ambient conditions (relative humidity, RH 50%), while the MAPI matrix-based PSCs were fabricated from N$_2$ atmosphere.[6,21] The concentrations of FAPI–PbS and MAPI–PbS were used as 1 mg mL^{-1} in both FAPI and MAPI matrices; all the photovoltaic characteristics such as best values and average of the devices are statistically evaluated in Figure S13–S14 and Table S6, Supporting Information. The device statistical parameters were collected from the 15 individual PSCs for each variable used. Figure S13–S14, and Table S6, Supporting Information, show the statistical photovoltaic parameters of all the perovskite matrix combinations with various PbS QD shells used. Interestingly, the FAPI–PbS–F devices achieved a higher average PCE of 18.9%, with a champion PCE of 21.3%, see Figure 6b and S13, Supporting Information, compared to the reference FAPI-based PSCs, which showed a champion PCE of 17.9%. The narrower distribution of PCEs in FAPI–PbS–F devices stands for good device reproducibility. The MAPI–PbS–F cells show lower V_{oc} and J_{sc} values which could be associated with the partial loss of photogenerated charges by transfer to PbS QDs and inherent thin film defects.[9a,30] The current–density voltage (J–V) scans of the FAPI matrix-based devices are shown in Figure 6f. The champion device from FAPI–PbS–F resulted in a short-circuit current density (J_{sc}) of 23.2 mA cm^{-2}, an fill factor (FF) of 0.81, a V_{oc} of 1.13 V, and a PCE of 21.3%, see Table S6, Supporting Information.

The photovoltaic parameters of MAPI, FAPI–PbS–M, and MAPI–PbS–M-based PSCs showed relatively lower device efficiency than the FAPI-based counterparts, see Figure S14 and Table S6, Supporting Information. For instance, the MAPI devices displayed PCE values with an average of 17%, with a champion PCE of 18.3%. The MAPI–PbS–M devices showed a lower average PCE value of 12.5%, with a champion PCE of 14.6%. Interestingly, the FAPI–PbS–M devices achieved a higher average PCE of 17.7%, with a champion PCE of 20.1%, see Figure 6b and S14, Supporting Information, and the PCEs were distributed in a very narrow range. The current–density voltage (J–V) scans of the MAPI matrix-based devices are shown in Figure 6f. The best device from FAPI–PbS–M achieved a champion PCE of 20.1% with a V_{oc} of 1.18 V, a J_{sc} of 21.2 mA cm^{-2}, and an FF of 0.80, see Table S6, Supporting Information. In addition, we measured the integrated current density from the incident photon-to-current efficiency (IPCE) over the spectral range from 300 to 850 nm. There is good agreement between the J_{sc} obtained from IPCE, see Figure 6f and S15, Supporting Information, and J–V curves, Table S6, Supporting Information, with an insignificant loss. We note that no substantial photocurrent can be contributed from the matrix embedded PbS QD absorption. The stabilized power outputs of the representative FAPI and MAPI matrix-based PSCs are compared in Figure S16, Supporting Information. The PSCs from FAPI–PbS–F and FAPI–PbS–M presented a power output of 20.7% and 19.5% respectively, after 1000 s of continuous illumination in the ambient atmosphere (RH of 55%).

To provide a theoretical interpretation to the reported experimental studies, we have further calculated the electronic levels in the vicinity of bandgap.[32] The electronic spectra of these atomic systems are depicted in **Figure 7**a–d. These spectra reveal a bandgap of about 1.7 eV, which is close to the ones measured with ultraviolet photoelectron spectroscopy (UPS), see Figure S17, Supporting Information, deep trap states ascribed to the dot surface, a PbS QD bandgap of about 2.4 eV, and hybridized states at the valence band (VB) maximum and conduction band (CB) minimum with contributions from perovskite matrix–I and PbS QD–S atomic species. Therefore, photogenerated carriers would occupy extended electronic states including the matrix and also the PbS QD and would recombine nonradiatively by the shown deep trap levels. Note that for computation time limitations very small PbS QDs are considered causing the significantly larger bandgap in comparison with bulk. Our computations confirm that the embedded PbS QDs may act as nonradiative recombination centers and effectively modulate the optoelectronic properties of these perovskite films. However, from the calculations alone we cannot deduce why the optical and electronic properties of the FAPI–PbS and MAPI–PbS differ.

To elucidate how the FAPI–PbS and MAPI–PbS shells influence the band structure of the FAPI and MAPI matrices, UPS were performed, Figure S17, Supporting Information. Electronic properties of the modified FAPI and MAPI films are summarized in Table S7, Supporting Information. By introducing FAPI–PbS and MAPI–PbS shells into FAPI matrix, the relative VB and CB energy positions are displaced to more positive values in vacuum scale, see Figure 7e. More specifically, S atoms from perovskite–PbS QD shell are incorporated in halide vacancies in both perovskite matrices, generating mainly a variation of electronic states coming from the VB and CB, inducing alterations in the corresponding band structure. Then, a

ADVANCED
SCIENCE NEWS
www.advancedsciencenews.com

Solar
RRL
www.solar-rrl.com
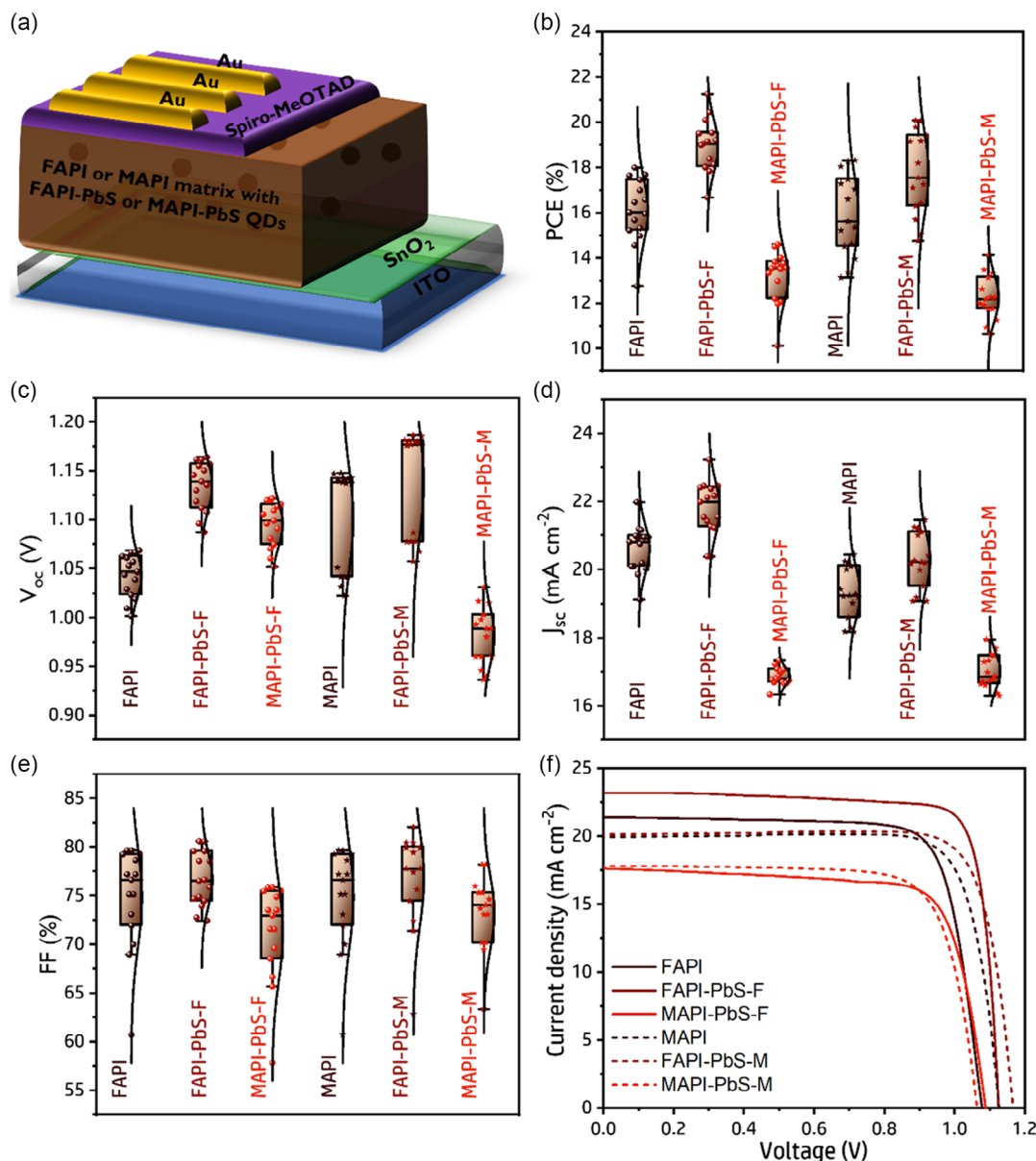
Figure 6. a) Schematics of PSC architecture. Box charts depicting statistics of b) PCE, c) V_{oc}, d) J_{sc}, e) FF, and f) J–V curves of FAPI, FAPI–PbS–F, MAPI–PbS–F, MAPI, FAPI–PbS–M, and MAPI–PbS–M-based PSCs. All the parameters were collected from 15 individual devices.

discrepancy in the S content is achieved after exposing the FAPI and MAPI films under ambient air after 1 month, see Table S3, Supporting Information, depicting a higher fraction of SO_4^{2-} in MAPI–PbS–F film than that of FAPI–PbS–F film; even both systems show the same amount of perovskite–QD shell added during perovskite preparation. Considering that MAPI films and the MAPI–PbS shell are prepared in presence of DMSO, we suggest that more sulfur and oxygen species will be contained into as-prepared perovskite films, also affecting the VB and CB positions, since DMSO can produce Pb complex in the perovskite structure.[33]

In this context, the presence of a higher S content from MAPI–PbS shell would promote a better energy offset in the

FAPI matrix to achieve a suitable band alignment with the charge transporter layers, for example, ITO/SnO$_2$ (4.7/4.5 eV) and spiro-MeOTAD/Au (5.22/5.1 eV), generating the highest V_{oc} in PSCs and improving the device performance. Nevertheless, MAPI–PbS–F film shows a higher density of defect sites than that of FAPI–PbS–F film (MAPI ligand from the shell can provide instability to the composite, due to fast MAI release compared to FAI), which increases the adsorbed oxygen content, restrains the carrier mobility, and decreases the solar cell performance. On the other hand, the presence of DMSO and MAI release can explain the similarity in the band structure and a low performance for MAPI, MAPI–PbS–M-based films, as in the case of MAPI–PbS–F system. Interestingly, although FAPI–PbS–M film shows
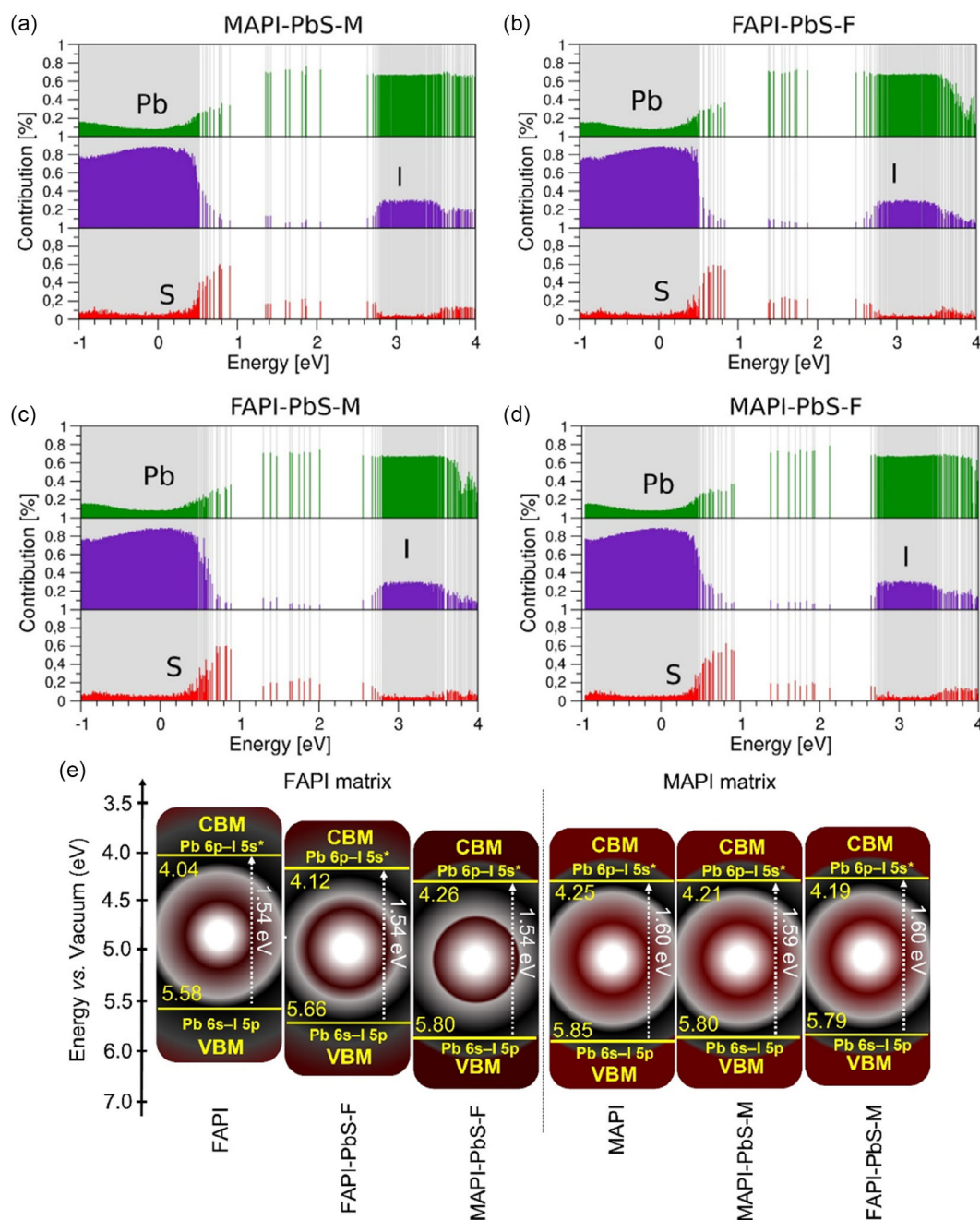
Figure 7. Electronic energy levels in a) MAPI–PbS–M, b) FAPI–PbS–F, c) FAPI–PbS–M, and d) MAPI–PbS–F perovskite systems, with indication of Pb, I, and S contributions given in green, blue, and red, respectively. Gray color sums up all the atomic contributions (100%). e) Band structure estimated from UPS parameters, see Table S7, Supporting Information, for FAPI and MAPI matrix-based perovskite thin films with embedded FAPI–PbS and MAPI–PbS QDs.

almost identical relative band positions than that of its MAPI analogous, the performance is higher and closer to the device containing the FAPI–PbS–F layer. This is related to the incorporation of FAPI ligand through PbS QDs shell, thus, mitigating the formation of a high density of halide defects in the MAPI matrix, which provides better stability and carrier transfer through the device. In this case, a reduced loss of carriers increases the V_{oc}, being pivotal to obtain highly efficient PSCs devices. At glance, Table S8, Supporting Information, depicts the effect of FAPI–PbS and MAPI–PbS QDs on structural, photophysical, and optoelectronic properties of the perovskite thin films.

3. Conclusion

In summary, we studied the influence of adding PbS QDs with HP shells (FAPI–PbS and MAPI–PbS) to FAPI and MAPI thin films on the perovskite crystallinity, strain, morphology, optoelectronic properties, and material stability. It has been observed that the PbS QDs exert a compressive strain in the FAPI perovskite matrix. In contrast, the lattice expansions by the embedded PbS QDs are responsible for the small octahedral distortions in the MAPI matrix. We observed that MAPI–PbS–F films experienced stronger non–radiative recombination processes by photogenerated charge transfer to the PbS QDs, which is reflected in decreased optical properties with respect to the reference FAPI films. On the contrary, enhanced photophysical properties are observed for FAPI–PbS–M with PLQY value of 0.253 in comparison to 0.211 for MAPI films, which are related to the better perovskite crystallinity, leading to reduced nonradiative recombination. Moreover, we observe the amalgamation of sulfur atoms from embedded PbS QDs to fill/compensate halide deficiency, which eventually hampers the film oxidation in ambient atmosphere and concomitantly boosts the longevity of the hybrid perovskite thin films. Finally, we fabricated the PSCs from the composite films. The champion PSCs from FAPI–PbS–F and FAPI–PbS–M achieved PCEs up to 21.3% and 20.1%, respectively, with a stable performance in the ambient atmosphere. Finally, we corroborated the influence of PbS QD shells on the perovskite bulk energy level modification through the combined theoretical and experimental studies. We showed that variations in photophysical and optoelectronic performances are associated with the partial changes in energy-level offset by the monolayer capping layer on PbS QDs and that the FAPI shell is needed to obtain the best energy alignment and in turn achieve high solar cell efficiencies. By demonstrating the impact of the shell of the PbS QDs additive and subsequent structural and optoelectronic properties of FAPI and MAPI perovskite films, this work opens a platform for further fundamental understanding of this strategy to other metastable perovskite materials. PbS additives can be effectively used to tune the properties of HP films causing both the increase of photoconversion efficiency and film stability. This work opens the door to further control the property tuning by the use of tailored optimized shells.

4. Experimental Section

Materials and Methods: All the materials were used without any further purification procedures. Methylammonium iodide (MAI, 98%, from GreatCell solar), formamidinium iodide (FAI, 98%, from GreatCell solar), lead iodide (PbI$_2$, >98%, from TCI), dimethyl sulfoxide (DMSO, anhydrous, 99.9%), N,N-dimethylformamide (DMF, Anhydrous, 99.9%), N-Methyl-2-pyrrolidone (NMP, Anhydrous, 99.9%), ethyl acetate (Anhydrous, 99.8%), diethyl ether (Anhydrous, >99.8%), Chlorobenzene (CB, Anhydrous, 99.8%), 4-*tert*-butylpiridine (tBP, 96%), acetonitrile (MeCN, Anhydrous, 99.8%), lithium bis(trifluoromethylsulfonyl)imide (Li-TFSI, 99.95%), hydrochloric acid (HCl, 37%), and zinc powder (99.995%) were from Sigma Aldrich. Ethanol and acetone were from PanReac, 2-isopropanol (99.7% from Carlo Erba), 2,20,7,70-tetrakis[N,N-di(4-methoxyphenyl)amino]-9,90-spirobifluorene (Spiro-MeOTAD 99% from Feiming chemical limited), toluene (Anhydrous 99.8%) were from VWR, and octane and SnO$_2$ colloid precursor from Alfa Aesar (15% in

H$_2$O colloidal dispersion). Indium tin oxide (ITO)-coated glass substrates (Pilkington TEC-15, ≈15 Ω sq^{-1}) were used for the fabrication of PSCs.

Ligand Exchange Procedure of PbS QDs: The PbS QDs were synthesized according to the reported procedure.[5b,6] For the ligand exchange with FAPI and MAPI perovskite precursor ions, a 0.25 M of FAPI or MAPI solution (in DMF) and 10 mg mL^{-1} of PbS QDs solution (in octane) were mixed in an equal volume ratio (v/v of 1:1) and stirred for 30 min at 30 °C (stirred at room temperature for MAPI ligand exchange process). The PbS QDs were transferred from the nonpolar-octane phase to the polar-DMF phase. Following this, the DMF phase was washed three times with octane to remove the excess oleic acid organic ligands. Then, the ligand-exchanged PbS QDs (named as FAPI–PbS and MAPI–PbS) were precipitated by the addition of antisolvent, for example, toluene. Finally, FAPI–PbS and MAPI–PbS were dried under vacuum for 2 h. The concentration of various ligand-exchanged PbS QDs (hereafter named as FAPI–PbS and MAPI–PbS) used in perovskite solutions was 1 mg mL^{-1}, similar to the methodologies adopted earlier.[5b,6] For this study, we used two types of perovskite matrices, that is, both FAPI and MAPI systems with the incorporation of ligand-exchanged FAPI–PbS and MAPI–PbS QDs.

Perovskite Solar Cell Fabrication: The indium tin oxide (ITO)-coated glass substrates were etched with Zn powder and hydrochloric acid and followed by 10 min of ultrasonication bath cleaning with decon soap solution, deionized water, acetone, and isopropanol. SnO$_2$ was deposited by spin coating of colloidal SnO$_2$ (2.65 wt%) at 3000 rpm for 40 s, and the substrates were further annealed at 150 °C for 30 min. The FAPI perovskite solution was prepared by dissolving 461 mg of PbI$_2$ (1 mmol) and 172 mg of FAI (1 mmol), 96.30 µL of N-methyl-2-pyrrolidone (NMP, 1 mmol) in N,N-dimethylformamide (DMF, 590.71 µL), and the solution was heated at 60 °C.[1] The MAPI perovskite solution was prepared by dissolving 613 mg of PbI$_2$ (1.33 mmol) and 211 mg of MAI (1.33 mmol) in dimethyl sulfoxide (DMSO, 1000 µL) and the solution was heated at 70 °C. The dried FAPI–PbS and MAPI–PbS QDs were dispersed in 400 µL of DMF:NMP (for the FAPI based perovskite films) or DMSO (for the MAPI-based perovskite films) solvents to get a 25 mg mL^{-1} of stock solution. The stock solution was further diluted for the preparation of 1 mg mL^{-1} solution. The FAPI-based perovskite thin films were spin coated at 5000 rpm for 17 s and 500 µL of diethyl ether solution was dripped at 8th second. Subsequently, the substrates were annealed at 100 °C for 1 min and 165 °C for 10 min. The MAPI-based perovskite thin films were spin coated by the two-step spinning process, by 2000 rpm for 10 s and 6000 rpm for 30 s; 300 µL of ethyl acetate solution was dripped at 25th second. Then the substrates were annealed at 130 °C for 10 min. The Spiro-MeOTAD solution was deposited by spin coating at 4000 rpm for 35 s. The Spiro-MeOTAD solution was prepared by dissolving 72.3 mg of spiro-MeOTAD in 1 mL chlorobenzene, *tert*-butyl pyridine (t-BP, 28.8 µL), and lithium bis(trifluoromethylsulfonyl) imide (Li-TFSI, 17.5 µL from a stock solution of 520 mg in 1 mL of acetonitrile). Finally, 90 nm of the gold counter electrode was deposited using a thermal evaporator. Note that the FAPI-based perovskite and Spiro-MeOTAD thin films were deposited at ambient atmospheric conditions (with a relative humidity of ≈35–55%). However, the fabrication of PSCs and thin films based on the MAPI matrix was carried out in N$_2$ atmosphere with a single-step deposition procedure.[21]

X-ray Diffraction (XRD): The crystallographic information of the films was analyzed by an X-ray diffractometer (D8 Advance, Bruker AXS) (Cu Kα, the wavelength of *l* = 1.5406 Å) within the range of 10°–55° with a step size of 0.02°. The XRD patterns were recorded from films deposited atop the ITO/SnO$_2$ substrates.

Raman Spectroscopy: The micro-Raman spectra were measured by WiTec apyron equipment at 532 nm excitation wavelength and signals were collected with an EMCCD detector. The laser power intensity used was 0.1 mW. The Raman measurements were conducted in ambient air conditions with an RH of 40–55%. The Raman spectra were shown without any spectral correction or normalization and the vertical lines indicated spectral mode assignment. The samples were fabricated on ITO/SnO$_2$ substrates. Raman spectra measurements were carried out in ambient air atmosphere with an excitation wavelength of 532 nm laser and 0.1 mW power.

Scanning Electron Microscope (SEM): The topographical and cross-sectional images were recorded by field-emission scanning electron microscope (SEM) JEOL 3100F) operated at 5 kV. The SEM was recorded from films deposited on top of the ITO substrate.

Electron Backscattered Diffraction (EBSD): The EBSD patterns of perovskites deposited on ITO/SnO_2 were collected with an EDAX Clarity direct detection system mounted on a FEI Verios 460 SEM. The samples were mounted on an aluminum stub with silver paste. The sides of the samples were covered with silver paste to further connect the perovskite layer and the aluminum stub. During the measurements, the samples were tilted a 70° angle relative to the horizontal. Kikuchi patterns were collected at a working distance of 8.2–13.2 mm from the electron beam source, using an accelerating voltage of 10 kV, low current of 100 pA, in a hexagonal grid with a step size of 20 nm. The exposure pixel dwell time was 50 ms for all FAPI-based films and 100–200 ms for the MAPI-based films. Data analysis of the Kikuchi patterns was performed using the EDAX OIM software, making use of neighboring grain averaging to increase the pattern intensity and CI standardization clean up to increase the number of well-indexed points without changing their orientation. The crystal structures used for indexing the Kikuchi patterns were tetragonal for the MAPI matrices (space group *I4/mcm*, $a = 8.844$ Å and $c = 12.63$ Å), cubic for the FAPI matrices (space group *Pm-3m*, $a = 6.361$ Å), and trigonal in case PbI_2 was present (space group *P-3m1*, $a = 4.59$ Å, $c = 6.78$ Å).

X-ray Photoelectron Spectroscopy: Surface chemical composition and electronic state of modified FAPI and MAPI films were determined by XPS (ESCA-2R, Scienta-Omicron). Spectra were recorded using monochromatic Al Kα = 1486.6 eV. The following sequence of spectra was recorded: survey spectra, C 1s, Pb 4f, I 3d, O 1s, S 2p, and C 1s again to verify the stability of the charge as the function of time. The survey and HR spectra were recorded at a pass energy of 150 and 20 eV, respectively. Binding energy scale was referenced to adventitious carbon (284.8 eV). CasaXPS processing software (Casa software Ltd) was used to analyze the data and the quantitative analysis was made using sensitivity factors provided by the manufacturer. On the other hand, work function, VB maximum, and ionization energy were determined by UPS performed in an UHV platform (ESCA, 2SR, Scienta-Omicron). UPS spectra were taken with HeI (21.2 eV) UV light and recorded with a constant pass energy of 3.0 eV. The samples were biased to −10 V during each measurement in order to measure the secondary-electron cutoff. The obtained UPS spectra were first referenced to the Fermi edge (0 eV) of a gold blank.

UV–Vis Spectra: The absorption spectra were obtained using a UV/Vis absorption spectrophotometer (Varian, Cary 300). The UV–vis spectra were recorded from films deposited on top of the quartz glass substrate.

Steady-State PL: A 405 nm laser diode (Thorlabs S1FC405) at a power output of 1.08 mW was used as the excitation source of samples deposited on quartz. A long-pass filter, LP532, was used to remove the excitation laser from the signal. The PL was coupled into a fiber connected to an OceanOptics USB4000 spectrometer. An integration time of 500 ms was used for each measurement.

Photoluminescence Quantum Yield (PLQY): The PLQY was measured by using a custom-modified GPS-033-SL integrating sphere built by LabSphere. A 405 nm laser diode (Thorlabs S1FC405) at a power output of 0.4 mW (0.16 W cm^{-2}) was used as the excitation source of samples deposited on quartz, passing through optical chopper (Thorlabs, MC2000B-EC) running at 40 Hz, hitting the sample into the integrating sphere. After hitting the sample, the light left the exit port of the sphere fitted with a baffle to prevent direct reflections and hit onto a low-noise Newport 818-SL-calibrated photodetector which was connected to a Stanford Research Systems SR830 lock-in amplifier. We measured the excitation and emission separately. The excitation was measured using a short-pass filter (Thorlabs FESH0450). A combination of a long-pass filter, LP532, and a short-pass filter, FES950, in front of the photodetector was used to remove the excitation laser and the contribution of the PbS emission from the signal. The comparison of the two measured quantities resulted in quantum yield. The sensitivity as a function of wavelength was calibrated with the responsivity of the photodetector.

Time-Correlated Single-Photon Counting (TCSPC): Time-correlated single-photon counting (TCSPC) se-built setup equipped with PicoQuant PDL 828 "Sepia II" and a PicoQuant HydraHarp 400 multichannel pico-second event timer and TCSPC module. A 485 nm pulsed laser (PicoQuant LDH-D-C-640) at a power of 0.01 mW with a repetition rate of 10 MHz and 5 MHz was used to excite the MAPI- and FAPI-based samples, respectively. A combination of a long-pass filter, LP450, a notch filter, ZET488NF, and a short-pass filter, FES950, were placed in front of the detector to remove the excitation laser and the contribution of the PbS emission from the signal. The lifetime traces were acquired in the course of 5 min each. The TRPL measurements were studied on quartz glass substrates and all the PL decay curves were fitted with a single-exponential decay function to acquire the lifetime (τ) values.

Solar Cell Characterization: The current–voltage (*J–V*) curves were measured using a Keithley 2612 source meter under AM 1.5G (1000 Wm^{-2}) provided by a Solar Simulator Abet, Xenon short-arc lamp Ushio 150 watts, in the air (at room temperature, ≈25 °C) and without encapsulation. Each *J–V* curve was generated from a starting potential of 1.2 V to a final potential of −0.02 V (reverse scan; vice versa for the forward scan) using a scan rate of 10 mVs^{-1}. The active area of the cell was 0.121 cm^2.

Supporting Information

Supporting Information is available from the Wiley Online Library or from the author.

Conflict of Interest

The authors declare no conflict of interest.

Author Contributions

S.M. and I.M.S. conceived the idea and oversaw the project. K.M.M.S., C.J.T.G., and R.A.M.G. carried out device fabrication and characterization under the supervision of S.M. and M.E.R.G. A.F.G.-R. synthesized and characterized the PbS quantum dots. L.A.M. and I.S. carried out electron backscatter diffraction and interpreted the data under the supervision of B.E. L.A.M. performed the optical absorption, photoluminescence, and time-resolved photoluminescence experiments under the supervision of B.E. J.R.P. carried out the X-ray photoelectron spectroscopy measurements and interpreted the data. S.M. and K.M.M.S. wrote the manuscript. All the authors are involved in the discussion on data analysis and contributed to manuscript preparation.

Data Availability Statement

The data that support the findings of this study are available from the corresponding author upon reasonable request.

[1] a) A. K. Jena, A. Kulkarni, T. Miyasaka, *Chem. Rev.* **2019**, *119*, 3036; b) National Renewable Energy Laboratory, Best Research-Cell Efficiency Chart, https://www.nrel.gov/pv/cell-efficiency.html (accessed: December 2023); c) A. Al-Ashouri, E. Köhnen, B. Li, A. Magomedov, H. Hempel, P. Caprioglio, J. A. Márquez, A. B. M. Vilches, E. Kasparavicius, J. A. Smith, N. Phung, D. Menzel, M. Grischek, L. Kegelmann, D. Skroblin, C. Gollwitzer, T. Malinauskas, M. Jošt, G. Matič, B. Rech, R. Schlatmann, M. Topič, L. Korte, A. Abate, B. Stannowski, D. Neher, M. Stolterfoht, T. Unold, V. Getautis, S. Albrecht, *Science* **2020**, *370*, 1300; d) J. Jeong, M. Kim, J. Seo, H. Lu, P. Ahlawat, A. Mishra, Y. Yang, M. A. Hope, F. T. Eickemeyer, M. Kim, Y. J. Yoon, I. W. Choi, B. P. Darwich, S. J. Choi, Y. Jo, J. H. Lee, B. Walker, S. M. Zakeeruddin, L. Emsley, U. Rothlisberger, A. Hagfeldt, D. S. Kim, M. Grätzel, J. Y. Kim, *Nature* **2021**, *592*, 381.

[2] a) S. D. Stranks, G. E. Eperon, G. Grancini, C. Menelaou, M. J. P. Alcocer, T. Leijtens, L. M. Herz, A. Petrozza, H. J. Snaith, *Science* **2013**, *342*, 341; b) K. M. M. Salim, E. Hassanabadi, S. Masi, A. F. Gualdrón-Reyes, M. Franckevicius, A. Devižis, V. Gulbinas, A. Fakharuddin, I. Mora-Seró, *ACS Appl. Electron. Mater.* **2020**, *2*, 2525; c) Y. C. Kim, K. H. Kim, D.-Y. Son, D.-N. Jeong, J.-Y. Seo, Y. S. Choi, I. T. Han, S. Y. Lee, N.-G. Park, *Nature* **2017**, *550*, 87; d) I. Suárez, E. J. Juárez-Pérez, J. Bisquert, I. Mora-Seró, J. P. Martínez-Pastor, *Adv. Mater.* **2015**, *27*, 6157.

[3] a) S. Rakshit, P. Piatkowski, I. Mora-Seró, A. Douhal, *Adv. Opt. Mater.* **2022**, *10*, 2102566; b) T. T. Ngo, I. Mora-Seró, *J. Phys. Chem. Lett.* **2019**, *10*, 1099.

[4] T. T. Ngo, S. Masi, P. F. Mendez, M. Kazes, D. Oron, I. M. Seró, *Nanoscale Adv.* **2019**, *1*, 4109.

[5] a) M. Liu, Y. Chen, C.-S. Tan, R. Quintero-Bermudez, A. H. Proppe, R. Munir, H. Tan, O. Voznyy, B. Scheffel, G. Walters, A. P. T. Kam, B. Sun, M.-J. Choi, S. Hoogland, A. Amassian, S. O. Kelley, F. P. García de Arquer, E. H. Sargent, *Nature* **2019**, *570*, 96; b) S. Masi, C. Echeverría-Arrondo, K. M. M. Salim, T. T. Ngo, P. F. Mendez, E. López-Fraguas, D. F. Macias-Pinilla, J. Planelles, J. I. Climente, I. Mora-Seró, *ACS Energy Lett.* **2020**, *5*, 418.

[6] K. M. M. Salim, S. Masi, A. F. Gualdrón-Reyes, R. S. Sánchez, E. M. Barea, M. Krečmarová, J. F. Sánchez-Royo, I. Mora-Seró, *ACS Energy Lett.* **2021**, *6*, 3511.

[7] a) E. A. Gaulding, X. Chen, Y. Yang, S. P. Harvey, B. To, Y.-H. Kim, M. C. Beard, P. C. Sercel, J. M. Luther, *ACS Mater. Lett.* **2020**, *2*, 1464; b) M. Albaladejo-Siguan, D. Becker-Koch, A. D. Taylor, Q. Sun, V. Lami, P. G. Oppenheimer, F. Paulus, Y. Vaynzof, *ACS Nano* **2020**, *14*, 384.

[8] a) Z. Ning, X. Gong, R. Comin, G. Walters, F. Fan, O. Voznyy, E. Yassitepe, A. Buin, S. Hoogland, E. H. Sargent, *Nature* **2015**, *523*, 324; b) X. Zhang, J. Zhang, D. Phuyal, J. Du, L. Tian, V. A. Öberg, M. B. Johansson, U. B. Cappel, O. Karis, J. Liu, H. Rensmo, G. Boschloo, E. M. J. Johansson, *Adv. Energy Mater.* **2018**, *8*, 1702049; c) S.-S. Li, C.-H. Chang, Y.-C. Wang, C.-W. Lin, D.-Y. Wang, J.-C. Lin, C.-C. Chen, H.-S. Sheu, H.-C. Chia, W.-R. Wu, U. S. Jeng, C.-T. Liang, R. Sankar, F.-C. Chou, C.-W. Chen, *Energy Environ. Sci.* **2016**, *9*, 1282.

[9] a) P. Piatkowski, S. Masi, P. Galar, M. Gutiérrez, T. T. Ngo, I. Mora-Seró, A. Douhal, *J. Mater. Chem. C* **2020**, *8*, 14834; b) P. Galar, P. Piatkowski, T. T. Ngo, M. Gutiérrez, I. Mora-Seró, A. Douhal, *Nano Energy* **2018**, *49*, 471.

[10] W.-T. Wang, P. Chen, C.-H. Chiang, T.-F. Guo, C.-G. Wu, S.-P. Feng, *Adv. Funct. Mater.* **2020**, *30*, 1909755.

[11] a) B. L. Watson, N. Rolston, A. D. Printz, R. H. Dauskardt, *Energy Environ. Sci.* **2017**, *10*, 2500; b) Y. Chen, Y. Lei, Y. Li, Y. Yu, J. Cai, M.-H. Chiu, R. Rao, Y. Gu, C. Wang, W. Choi, H. Hu, C. Wang, Y. Li, J. Song, J. Zhang, B. Qi, M. Lin, Z. Zhang, A. E. Islam, B. Maruyama, S. Dayeh, L.-J. Li, K. Yang, Y.-H. Lo, S. Xu, *Nature* **2020**, *577*, 209; c) C. Zhu, X. Niu, Y. Fu, N. Li, C. Hu, Y. Chen, X. He, G. Na, P. Liu, H. Zai, Y. Ge, Y. Lu, X. Ke, Y. Bai, S. Yang, P. Chen, Y. Li, M. Sui, L. Zhang, H. Zhou, Q. Chen, *Nat. Commun.* **2019**, *10*, 815.

[12] Y.-H. Deng, L. G. Nest, *J. Microsc.* **2021**, *282*, 195.

[13] T. W. Jones, A. Osherov, M. Alsari, M. Sponseller, B. C. Duck, Y.-K. Jung, C. Settens, F. Niroui, R. Brenes, C. V. Stan, Y. Li, M. Abdi-Jalebi, N. Tamura, J. E. Macdonald, M. Burghammer, R. H. Friend, V. Bulović, A. Walsh, G. J. Wilson, S. Lilliu, S. D. Stranks, *Energy Environ. Sci.* **2019**, *12*, 596.

[14] M. T. Weller, O. J. Weber, J. M. Frost, A. Walsh, *J. Phys. Chem. Lett.* **2015**, *6*, 3209.

[15] X. Zheng, C. Wu, S. K. Jha, Z. Li, K. Zhu, S. Priya, *ACS Energy Lett.* **2016**, *1*, 1014.

[16] a) G. Kim, H. Min, K. S. Lee, D. Y. Lee, S. M. Yoon, S. I. Seok, *Science* **2020**, *370*, 108; b) C. Echeverría-Arrondo, K. M. M. Salim, S. Masi, I. Mora-Seró, *Adv. Phys. Res.* **2023**, *2*, 2200079.

[17] H. Sun, G. W. P. Adhyaksa, E. C. Garnett, *Adv. Energy Mater.* **2020**, *10*, 2000364.

[18] C. Ma, F. T. Eickemeyer, S.-H. Lee, D.-H. Kang, S. J. Kwon, M. Grätzel, N.-G. Park, *Science* **2023**, *379*, 173.

[19] a) K. P. McKenna, *ACS Energy Lett.* **2018**, *3*, 2663; b) S. Cai, J. Dai, Z. Shao, M. U. Rothmann, Y. Jia, C. Gao, M. Hao, S. Pang, P. Wang, S. P. Lau, K. Zhu, J. J. Berry, L. M. Herz, X. C. Zeng, Y. Zhou, *J. Am. Chem. Soc.* **2022**, *144*, 1910.

[20] S. Jariwala, H. Sun, G. W. P. Adhyaksa, A. Lof, L. A. Muscarella, B. Ehrler, E. C. Garnett, D. S. Ginger, *Joule* **2019**, *3*, 3048.

[21] P. F. Méndez, S. K. M. Muhammed, E. M. Barea, S. Masi, I. Mora-Seró, *Sol. RRL* **2019**, *3*, 1900191.

[22] M. Ledinský, P. Löper, B. Niesen, J. Holovský, S.-J. Moon, J.-H. Yum, S. De Wolf, A. Fejfar, C. Ballif, *J. Phys. Chem. Lett.* **2015**, *6*, 401.

[23] a) P. Pistor, A. Ruiz, A. Cabot, V. Izquierdo-Roca, *Sci. Rep.* **2016**, *6*, 35973; b) G. Grancini, S. Marras, M. Prato, C. Giannini, C. Quarti, F. De Angelis, M. De Bastiani, G. E. Eperon, H. J. Snaith, L. Manna, A. Petrozza, *J. Phys. Chem. Lett.* **2014**, *5*, 3836.

[24] E. Mosconi, C. Quarti, T. Ivanovska, G. Ruani, F. De Angelis, *Phys. Chem. Chem. Phys.* **2014**, *16*, 16137.

[25] a) P. S. Whitfield, N. Herron, W. E. Guise, K. Page, Y. Q. Cheng, I. Milas, M. K. Crawford, *Sci. Rep.* **2016**, *6*, 35685; b) J. Breternitz, M. Tovar, S. Schorr, *Sci. Rep.* **2020**, *10*, 16613.

[26] a) G. Rajendra Kumar, A. Dennyson Savariraj, S. N. Karthick, S. Selvam, B. Balamuralitharan, H.-J. Kim, K. K. Viswanathan, M. Vijaykumar, K. Prabakar, *Phys. Chem. Chem. Phys.* **2016**, *18*, 7284; b) C. Rocks, V. Svrcek, P. Maguire, D. Mariotti, *J. Mat. Chem. C* **2017**, *5*, 902.

[27] K. Ho, M. Wei, E. H. Sargent, G. C. Walker, *ACS Energy Lett.* **2021**, *6*, 934.

[28] S. Rondon, P. M. A. Sherwood, *Surf. Sci. Spectra* **1998**, *5*, 97.

[29] F. M. Doyle, R. Woods, *Electrochemistry in Mineral and Metal Proc. VI: Proc. of the Int. Symp.*, The Electrochemical Society Inc., Paris, France **2003**.

[30] L. Gao, L. N. Quan, F. P. García de Arquer, Y. Zhao, R. Munir, A. Proppe, R. Quintero-Bermudez, C. Zou, Z. Yang, M. I. Saidaminov, O. Voznyy, S. Kinge, Z. Lu, S. O. Kelley, A. Amassian, J. Tang, E. H. Sargent, *Nat. Photonics* **2020**, *14*, 227.

[31] C. Witt, K. Schötz, M. Kuhn, N. Leupold, S. Biberger, P. Ramming, F.-J. Kahle, A. Köhler, R. Moos, E. M. Herzig, F. Panzer, *J. Phys. Chem. C* **2023**, *127*, 10563.

[32] a) J. Hutter, M. Iannuzzi, F. Schiffmann, J. VandeVondele, *WIREs Comput. Mol. Sci.* **2014**, *4*, 15; b) C. Giansante, I. Infante, *J. Phys. Chem. Lett.* **2017**, *8*, 5209; c) J. P. Perdew, K. Burke, M. Ernzerhof, *Phys. Rev. Lett.* **1996**, *77*, 3865.

[33] S. Rahimnejad, A. Kovalenko, S. M. Forés, C. Aranda, A. Guerrero, *ChemPhysChem* **2016**, *17*, 2795.